

Working surfaces in radiative, non-top hat jets

A.C. Raga¹, J. Cantó¹, and S. Cabrit²

¹ Instituto de Astronomía, UNAM, Ap. 70-264, 04510 D.F., México

² Observatoire de Paris, DEMIRM, URA 336 du CNRS, 61 Avenue de l’Observatoire, F-75014 Paris, France

Received 18 August 1997 / Accepted 18 December 1997

Abstract. Most models of radiative jets have been computed for the special case of a top hat initial cross section. This paper discusses the dynamics of both leading and internal working surfaces in jets with more general initial cross sections, based on both an analytic, “thin shell” model, and on a full numerical simulation. We find that a non-top hat cross section for the jet ram pressure first leads to a strong curvature of the working surface shocks, and at longer timescales to the formation of a warm, dense “nose cone”. These results have interesting implications for comparisons between radiative jet models and observations of Herbig-Haro objects.

Key words: ISM: jets and outflows – hydrodynamics – shock waves – methods: analytical

1. Introduction

Several years have now passed since the first numerical simulations of radiative Herbig-Haro (HH) jets were made (Falle, Innes & Wilson 1987; Raga 1988). During these years, several researchers have carried out such numerical simulations, studying different special cases and using different numerical techniques, computational resolutions, and microphysical descriptions.

Interestingly, most of these simulations (with the apparently exclusive exception of the models of Raga 1995 and Smith et al. 1997) have been computed for the case of jets with “top hat” initial cross sections. This of course does not imply that the cross sections of these jets further downstream still maintain the initial top hat profile. The two main effects that lead to a distortion of the initial, top hat cross section of the beam are:

- *the formation of incident and reflected shocks in the jet beam:* as discussed by Cantó, Raga & Binette (1989), the crossing shocks formed in radiative jets tend to be very oblique, so that they do not produce large velocity perturbations on the jet flow. On the other hand, these shocks can produce a quite substantial compression, leading to centrally or laterally peaked density cross sections for the jet beam

(depending on whether the cross section cuts a reflected or an incident shock, respectively),

- *the formation of a turbulent mixing layer, leading to a fully turbulent flow further downstream:* the Kelvin-Helmholtz instability at the beam/environment boundary leads to the formation of a turbulent mixing layer (Cantó & Raga 1991). This mixing layer grows downstream into the jet, eventually leading to the formation of a fully turbulent jet beam. Such turbulent jet beams show a centrally peaked velocity cross section, and a relatively uniform density cross section (see, e. g., Dash, Wolf & Seiner 1985; Falle 1994).

In the present paper, we discuss the dynamics of working surfaces (both leading and internal) in jets with non-top hat cross sections. These non-top hat cross sections could of course reflect either the direct effects of the jet production mechanism (particularly, in the regions closer to the source) or the effects on the jet beam resulting from the propagation of the jet in the surrounding environment (see above).

We first present a very simple, “thin shell” analytic model describing the propagation of leading and internal working surfaces in a radiative jet with a non-top hat cross section (Sect. 2). Secondly, we present the results of a numerical simulation of a particular flow (Sect. 3).

2. Thin shell working surface model

2.1. The separation between the working surface shocks

A working surface has two main shocks: a “jet shock” and a bow shock. It is straightforward to estimate the separation between these two shocks.

Let us consider the leading working surface in a jet with a top hat cross section, density ρ_j and velocity v_j moving into a stationary ambient medium of density ρ_e . Fig. 1 shows a schematic diagram of the working surface, as seen from a reference system moving with the velocity v_{ws} of the working surface. If the bow shock and the jet shock are strong, the (approximately uniform) pressure inside the working surface is given by:

$$P_0 = \rho_j v_1^2 = \rho_e v_2^2, \quad (1)$$

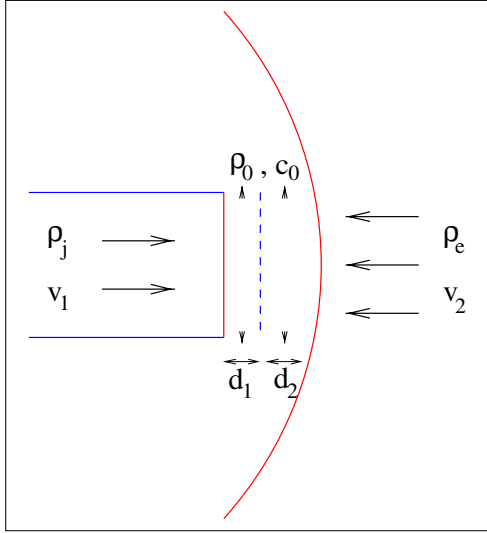


Fig. 1. Schematic diagram of a working surface at the head of a jet, seen from a reference frame moving with the velocity v_{ws} of the working surface. In this reference frame, the jet material enters the working surface with a velocity $v_1 = v_j - v_{ws}$ (where v_j is the jet velocity) and the environment enters with a velocity $v_2 = v_{ws}$. The material exits the working surface with a lateral sonic velocity c_0 . The contact discontinuity between the jet and environment material is shown with a dashed line.

where $v_1 = v_j - v_{ws}$ and $v_2 = v_{ws}$. If we assume that the post shock material rapidly cools to an isothermal sound speed c_0 , we then have an approximately uniform density $\rho_0 = P_0/c_0^2$ for the material in between the two working surface shocks.

The material in the working surface exits laterally with an approximately sonic velocity. If the working surface flow is in a stationary state, the mass entering through each shock (per unit time) has to be balanced by the mass ejected sideways. In other words, we have:

$$\pi r_j^2 \rho_j v_1 \approx 2\pi r_j d_1 \rho_0 c_0, \quad (2)$$

$$\pi r_j^2 \rho_e v_2 \approx 2\pi r_j d_2 \rho_0 c_0, \quad (3)$$

where d_1 and d_2 are the separations between the contact discontinuity and the jet shock and bow shock (respectively, see Fig. 1).

From Eqs. (1)-(3) we obtain:

$$d = d_1 + d_2 \approx \frac{(1 + \beta)^2}{2\beta} \frac{r_j}{M_j^0}; \quad \frac{d_1}{d_2} \approx \beta, \quad (4)$$

$$v_{ws} = \frac{\beta}{(1 + \beta)} v_j, \quad (5)$$

where $\beta = \sqrt{\rho_j/\rho_e}$ and the Mach number calculated with the jet velocity and the equilibrium sound speed is $M_j^0 = v_j/c_0$.

This simple estimate leads to the following conclusion. The high proper motions observed in HH jets imply that the value of β (=the square root of the jet to environment density ratio)

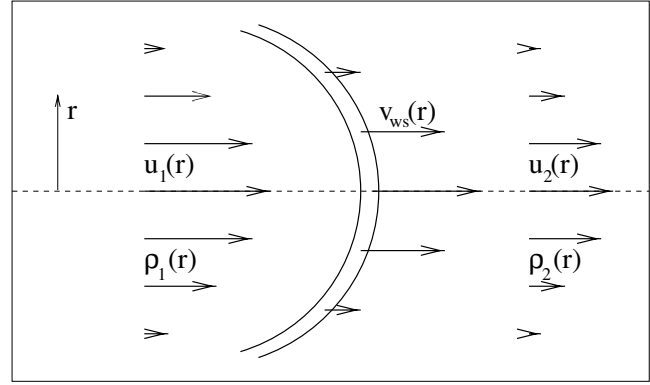


Fig. 2. Schematic diagram of an internal working surface in a jet with a non-top hat cross section. The working surface is formed through the interaction of material ejected with a radially dependent velocity $u_1(r)$ and density $\rho_1(r)$ with slower moving material of velocity $u_2(r)$ and density $\rho_2(r)$. The working surface moves forward with a radially-dependent velocity $v_{ws}(r)$ (see the text).

is generally not much smaller than unity, and in many objects has quite large values. This implies that the factor involving β in Eq. (1) is of order unity.

Also, the Mach numbers estimated for HH jets tend to be quite large, ranging from 10 to 30 or above. From Eq. (4) we then conclude that the separation d between the jet shock and the bow shock (see Fig. 1) is at least an order of magnitude smaller than the jet radius. Therefore, it is appropriate to model the working surface shocks with a “thin shell” approximation.

2.2. General method

Let us assume that the working surface is thin (compared to the jet radius, see above) and that the material going through the jet shock and the bow shock instantaneously mixes. In this “well mixed” approximation, the working surface can be described by considering simple momentum and mass conservation arguments.

Let us consider a perfectly collimated, cylindrically symmetric jet with time independent velocity and density cross sections given by $u_1(r)$, $\rho_1(r)$ (where r is the cylindrical radius, see Fig. 2) moving into an environment of velocity and density given by $u_2(r)$, $\rho_2(r)$. A parcel of working surface material presenting a unit surface area to the jet has a time-dependent mass $m(r, t)$, determined by the amount of material fed in through the jet and bow shocks:

$$m(r, t) = \{\rho_1(r) [u_1(r) - v_{ws}(r)] + \rho_2(r) [v_{ws}(r) - u_2(r)]\} t, \quad (6)$$

and a momentum which is given by:

$$\Pi(r, t) =$$

$$\{\rho_1(r) u_1(r) [u_1(r) - v_{ws}(r)] + \rho_2(r) u_2(r) [v_{ws}(r) - u_2(r)]\} t, \quad (7)$$

where $v_{ws}(r)$ is the velocity of the parcel of working surface material. Also, the momentum, mass and velocity of the parcel are related through the equation:

$$m(r, t) v_{ws}(r) = \Pi(r, t). \quad (8)$$

Using Eqs. (6)-(8), it is straightforward to determine the (radially varying) working surface velocity:

$$v_{ws}(r) = \frac{\beta(r) u_1(r) + u_2(r)}{1 + \beta(r)} \quad ; \quad \beta(r) = \sqrt{\frac{\rho_1(r)}{\rho_2(r)}}. \quad (9)$$

This relation can of course also be derived from ram pressure balance arguments.

As the working surface velocity is time-independent, we can find the shape of the working surface at a given time t simply by multiplying Eq. (9) by t . In the following two subsections we will discuss the shapes for the working surface obtained with two simple prescriptions for the jet and environmental cross sections.

2.3. Leading working surface

For a leading working surface moving into a stationary, uniform environment we have $u_2(r) = 0$, $\rho_2(r) = \rho_e$ (independent of r). Eq. (9) then takes the form:

$$v_{ws}(r) = \frac{\beta(r) u_1(r)}{1 + \beta(r)} \quad ; \quad \beta(r) = \sqrt{\frac{\rho_1(r)}{\rho_e}}. \quad (10)$$

where $u_1(r)$ and $\rho_1(r)$ are the velocity and density cross sections of the jet directly upstream of the working surface.

From Eq. (10) it is clear that for the case of a jet with a top hat density cross section (i. e., β independent of r), the velocity of the working surface (and hence its shape, which is obtained by multiplying v_{ws} by the time t , see above) directly follows the radial dependence of the jet velocity $u_1(r)$. Therefore, in the case of a jet with maximum velocity along the symmetry axis (as expected for a turbulent jet flow, see Sect. 1), we obtain a convex working surface, which becomes progressively more curved with increasing time.

For the case of a jet with a top hat velocity cross section, we expect the velocity (and shape) of the working surface to be proportional to $\beta(r)/[1 + \beta(r)]$ (see Eq. 10). It is easy to see that the working surface velocity is therefore a monotonically growing function of the square root of the jet to environment density ratio $\beta(r)$. Therefore, if the jet has a decreasing density with cylindrical radius, the working surface will take the standard, convex shape. On the other hand, if the jet has a cross section with density increasing away from the symmetry axis, a concave working surface is produced. As discussed in Sect. 1, both of these cases are possible in a jet which has developed internal crossing shocks in its beam.

For the high β case appropriate for many HH jets (see Sect. 1), Eq. (10) takes the form:

$$v_{ws}(r) \approx u_1(r) \left[1 - \frac{1}{\beta(r)} \right]. \quad (11)$$

We therefore see that for $\beta \gg 1$, the shape of the working surface is not strongly affected by the density cross section of the jet, and is mostly a direct reflection of the velocity cross section of the jet beam.

2.4. Internal working surface

Let us consider an internal working surface produced by a time change of the ejection velocity. The working surface is formed by faster material (of velocity u_1 and density ρ_1) catching up with slower material (of velocity u_2 and density ρ_2) ejected previously from the source.

In order to analyze the behaviour of Eq. (9) for this case, we assume that $u_1(r)$ and $u_2(r)$ have profiles that can be represented by a single radial function:

$$u_1(r) = u_{1,0} f(r), \quad (12)$$

$$u_2(r) = u_{2,0} f(r), \quad (13)$$

where $u_{1,0}$ and $u_{2,0}$ are constants and $f(0) = 1$.

Using (12) and (13), Eq. (9) can be written as:

$$\frac{v_{ws}(r)}{u_{1,0}} = \left[\frac{\alpha + \beta(r)}{1 + \beta(r)} \right] f(r), \quad (14)$$

where $\alpha = u_{2,0}/u_{1,0} < 1$ and $\beta(r) = \sqrt{\rho_1(r)/\rho_2(r)}$.

From Eq. (14) we again obtain that the working surface velocity is proportional to the velocity cross section of the jet, and that it is a monotonically increasing function of β . The same conclusions that we have obtained for a leading working surface (Sect. 2.c) therefore still apply.

2.5. The formation of a nose cone

The analytic working surface model presented in sections 2.b-d is based on the assumption that the material that has gone through the two shocks (at a given value of the cylindrical radius r) mixes instantaneously. This assumption of course does not result in a fully correct description of the flow.

The region in between the two working surface shocks will in principle contain a turbulent mixing layer. However, this mixing layer could be substantially thinner than the separation between the two shocks (Raga, Cabrit & Cantó 1995). The immediate postshock material which does not form part of the mixing layer will flow towards or away from the symmetry axis, depending on the curvature of the working surface.

For example, if we have a convex working surface, the material entering the bow shock is refracted away from the symmetry axis, while the material entering the jet shock is refracted towards the symmetry axis (the reverse being true for the case of a concave working surface). The convergence of the post-jet shock material stops the lateral, sonic outflow from the working surface (described in Sect. 2.1), so that material tends to

accumulate in the on-axis region, forming a “nose cone”. The formation of such structures has been previously observed in numerical simulations of radiative jet flows (see, e. g., Blondin, Fryxell & Königl 1990).

In the following section we present a numerical simulation of a non-top hat radiative jet flow. This simulation is then used to evaluate the applicability of the analytic model described above, and to show the eventual formation of a nose cone.

3. A numerical simulation

3.1. Parameters and numerical method

We have carried out an axisymmetric numerical simulation of a radiative jet with a non-top hat initial cross section. We have considered the case of a jet of initial radius $r_j = 7 \times 10^{15}$ cm moving into a homogeneous environment of number density (of atomic nuclei) $n_e = 50 \text{ cm}^{-3}$ and temperature $T_e = 10$ K. The jet is given an initial length of 10^{15} cm.

The jet has uniform initial density and temperature cross sections with a number density (of nuclei) $n_j = 500 \text{ cm}^{-3}$ and a temperature $T_j = 10$ K. The velocity has a non-top hat initial cross section, given by:

$$v_j(r) = \left[1 - 0.2 \left(\frac{r}{r_j} \right)^2 \right] \times 150 \text{ km s}^{-1}, \quad (15)$$

where r is the cylindrical radius.

The numerical simulation is carried out with the Coral gas-dynamic adaptive grid code (Raga 1994). The latest version of the code, which includes a detailed description of the ionization state of H, He, C, N, O, Ne and S, has been described in detail by Raga, Mellema and Lundqvist (1997) and by Mellema et al. (1998). For the present simulation, we have also included the treatment of the H_2 and CO molecules described by Raga et al. (1995).

The simulation is carried out on a 5-level binary adaptive grid giving a maximum resolution of 7.81×10^{13} cm and a minimum resolution of 1.25×10^{15} cm (in both the axial and radial directions). A reflection boundary condition has been used for the symmetry axis, and also for the boundary to the side of the injection jet cross section. The external axial and radial boundaries of the computational domain are never reached by the jet nor by the perturbed region of the environment.

In order to evaluate the appropriateness of the numerical resolution of our simulation, we first note that the initial jet radius is resolved with ≈ 90 points (at the highest resolution of the adaptive grid). Secondly, we note that the on-axis velocity of the bow shock is $\approx 114 \text{ km s}^{-1}$ (see Eq. 10). From the paper of Raga et al. (1997), we see that a 100 km s^{-1} shock moving into an atomic medium of number 50 cm^{-3} has a cooling distance (to 10^4 K) $d_c \approx 1.6 \times 10^{14}$ cm. This results in a marginal resolution of the on-axis post-bow shock cooling region of approximately 2 grid points. The recombination regions behind the jet shock and the lower velocity shocks in the bow shock wings are better resolved in our numerical simulation.

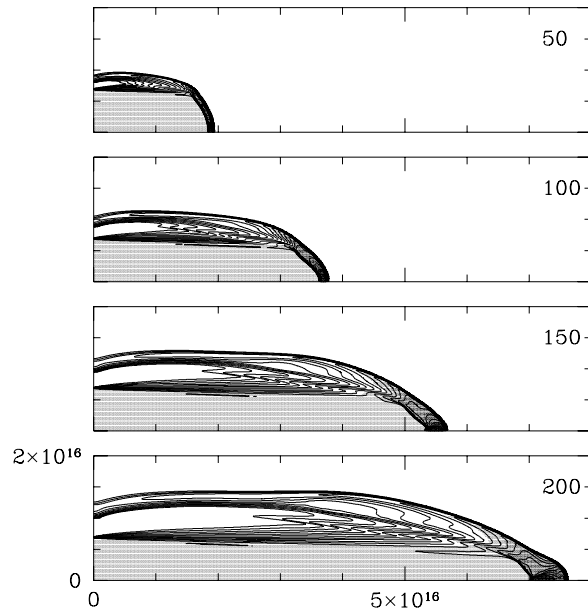


Fig. 3. Density stratification obtained for four different integration times (corresponding to $t = 50, 100, 150$ and 200 yr) from the numerical simulation described in the text. The stratification is shown with logarithmic, $2^{1/2}$ contours, as well as with a grey scale.

Finally, let us describe the initial atomic/molecular state of the gas. The environment is assumed to have fully molecular hydrogen, and a CO abundance (by number) equal to 10^{-4} times the abundance of H_2 . The jet is atomic, with neutral H, He, O, N and Ne and singly ionized C and S.

The numerical simulation has been carried out for a total integration time of 200 yr, after which the jet has developed a nose cone. The results obtained are described in the following sections.

3.2. Results

The density stratifications obtained from the simulation described in the previous section are shown in Fig. 3. Because of the centrally peaked, parabolic velocity profile (see Eq. 15), the working surface advances faster along the axis than along the edges of the jet beam, so that its shape becomes progressively more pointed. At early times (50-100 yr), the two working surface shocks limit a shocked “thin shell”, with a thickness that is considerably smaller than the jet radius. At later times (150-200 yr, see Fig. 3), an extended, dense plug begins to form on the symmetry axis. This is the “nose cone” described in Sect. 2.e.

The temperature stratifications of the region around the working surface are plotted in Fig. 4. Also plotted on the same figure are the loci for the working surface predicted from Eqs. (10) and (15). From this comparison, it is clear that at early times (50-100 yr), the analytic solution closely traces the highly compressed region between the two working surface shocks. At later times (150-200 yr, see Fig. 4), the developing nose cone produces an increased on-axis separation between the bow and

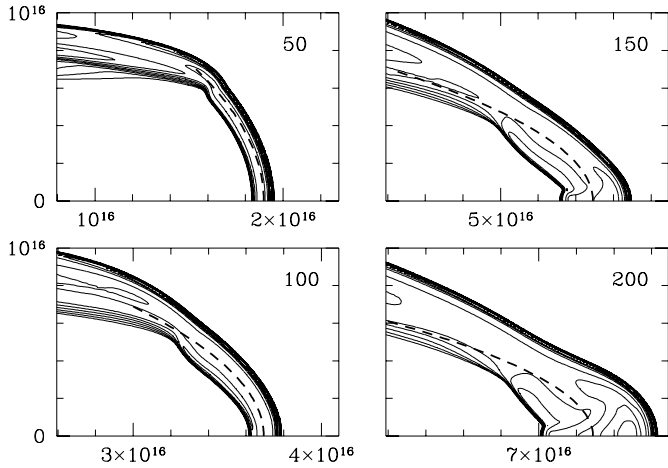


Fig. 4. Temperature stratification obtained for four different integration times (corresponding to $t = 50, 100, 150$ and 200 yr) from the numerical simulation described in the text (see also Fig. 3). Only the region close to the working surface is shown in the plots. The stratification is shown with logarithmic, $2^{1/2}$ contours (solid lines). The dashed lines represent the analytic, thin shell solution obtained for the same flow parameters (see the text).

jet shocks, introducing important differences between the analytic and numerical results. However, we find that the analytic and numerical solutions still agree relatively well for the bow shock wings (see Fig. 4).

In order to describe the physical properties of the nose cone that has formed at the $t = 200$ yr integration time (last panel of Figs. 3 and 4), in Fig. 5 we show pressure, temperature and density axial cuts through the working surface. In the region in between the two working surface shocks, the pressure has a value of $\log_{10} P = -8.0 \pm 0.5$ (where P is in dyn cm^{-2}). The temperature shows two peaks in the immediate post-jet and bow shock regions, separated by a relatively warm region with temperatures between 3500 and 10000 K. This warm region has a number density (of nuclei) ranging from approximately 10000 to 25000 cm^{-3} . Much larger density variations are of course seen in the steep cooling regions immediately behind the jet and bow shocks (see the bottom panel of Fig. 5).

3.3. Predicted images and comparisons with observations

In order to finalize our discussion of the numerical simulation of a non-top hat cross section jet, we present predictions of intensity maps for different emission lines, restricting ourselves to the case in which the outflow axis lies on the plane of the sky, and to the $t = 200$ yr integration stratification (see Fig. 5).

In Fig. 6, we show the predicted $H\alpha$ and [S II] 6717+31 images. The most dramatic feature is that while the $H\alpha$ map shows a completely dominant, single intensity peak in the on-axis region of the bow shock, the [S II] map shows a much broader high intensity region with two peaks. This extended, bright [S II] region corresponds to the warm “nose cone” material, which emits strongly in the [S II] lines but only weakly in

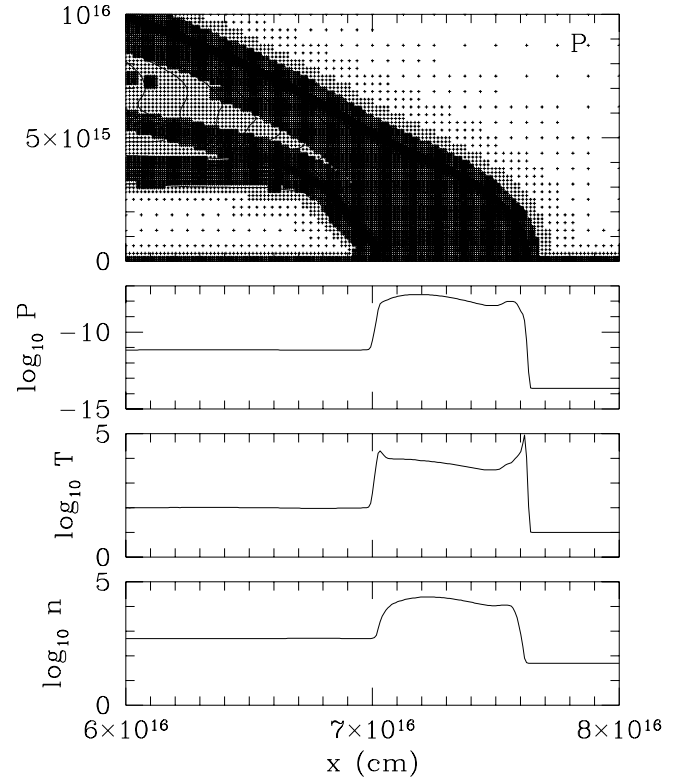


Fig. 5. Stratification obtained from the numerical simulation for the $t = 200$ yr integration time (see also Figs. 3 and 4). The top graph shows the pressure stratification (in logarithmic, $2^{1/2}$ contours), and the positions of the grid points selected by the adaptive grid algorithm. Only the region around the working surface of the jet is shown. The following graphs show cuts along the symmetry axis of the logarithms of the pressure P (in dyn cm^{-2}), temperature T (in K) and number density n of atomic nuclei (in cm^{-3}).

$H\alpha$. A qualitatively similar effect is seen in plane-parallel shock models (Raga & Binette 1991; Heathcote et al. 1996), where the far post-shock region of shocks with velocities $\sim 100 \text{ km s}^{-1}$ is seen to have a very high [S II]/ $H\alpha$ intensity ratio.

The second notable feature of Fig. 6 is the fact that the bow shock wings appear to be more extended in $H\alpha$ than in [S II]. This is in apparent disagreement with the predictions from plane shock models, in which the predicted [S II]/ $H\alpha$ ratio rapidly grows with decreasing shock velocities below 50 km s^{-1} (see, e. g., Hartigan, Raymond & Hartmann 1987). However, the extended “wing emission” seen in our numerical simulation is not formed in the recombination region behind the bow shock. This emission arises from the mixing layer between the jet and environment material, which has a locus internal to the locus of the bow shock. The difference in locus between the bow shock and the mixing layer is seen as an inwards radial shift of the wing of the $H\alpha$ emission (see Fig. 6).

In Fig. 7 we show the predicted $H\alpha$, H_2 1-0 s(1) and CO 2-1 images. A very clear trend is seen, with the $H\alpha$ emission being strongly concentrated towards the head of the bow shock, the H_2 1-0 s(1) emission peaking along the bow shock wings,

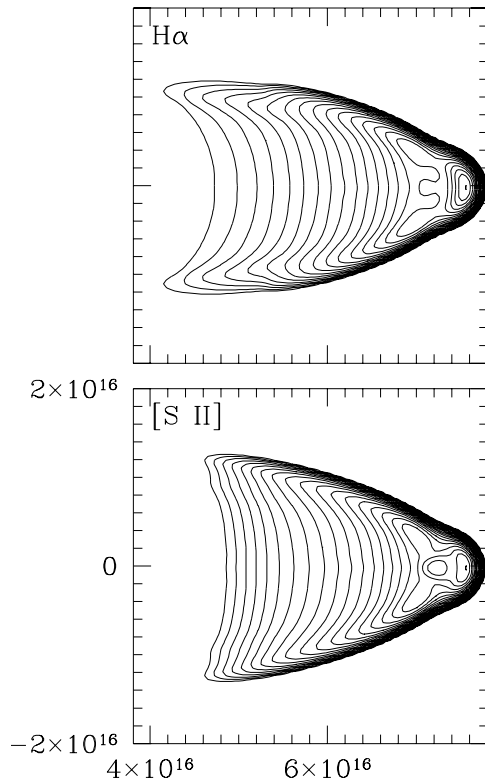


Fig. 6. $H\alpha$ (top) and $[S\ II]$ (bottom) maps predicted from the numerical simulation described in the text (also see Figs. 3-5) for a $t = 200$ yr integration time. The outflow is assumed to lie on the plane of the sky, and the maps have been convolved with a Gaussian point spread function of $\text{FWHM}=10^{15}$ cm to simulate the effects of the seeing. The contours correspond to successive factors of $2^{1/2}$ down from the peak intensity in the corresponding map.

and the CO 2-1 emission being concentrated even further away from the head, along the far bow shock wings.

These predictions can be compared qualitatively with observations of different Herbig-Haro (HH) objects. For example, the Hubble Space Telescope observations of HH 47A of Heathcote et al. (1996) show an extended, high $[S\ II]/H\alpha$ ratio emitting region trailing the bow shock. This region could correspond to a warm “nose cone”, such as the one obtained in our numerical simulation. A radiative working surface which does not develop such a nose cone would have a very small separation between the bow and jet shocks (see Sect. 2.a), so that it would not develop the extended $[S\ II]$ emitting region observed in HH 47A.

As in our numerical simulation the jet is atomic (i. e., not molecular), the molecular emission is only associated with the shocked environmental gas. An extended H_2 1-0 s(1) bow shock wing is observed for HH 1, in qualitative agreement with the results from our simulation (Davis, Eislöffel & Ray 1994; Noriega-Crespo & Garnavich 1994)

Interestingly, if the jet were molecular, and the jet shock velocity were lower than $\sim 30\text{ km s}^{-1}$, the warm nose cone would strongly emit in molecular lines. Future detections (or lack of detections) of such emitting structures would provide

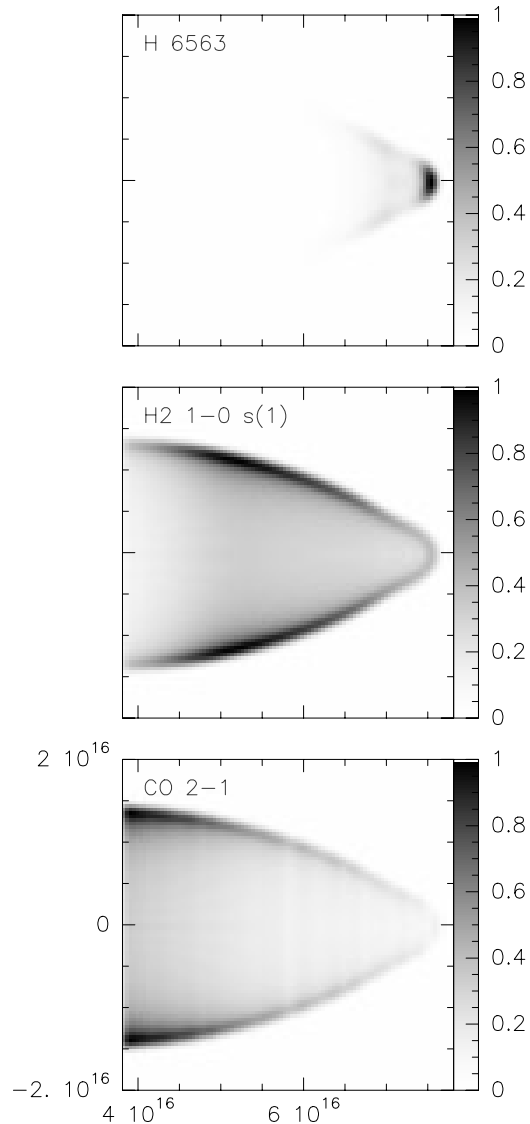


Fig. 7. $H\alpha$ (top), H_2 1-0 s(1) (centre) and CO 2-1 intensity maps predicted from the numerical simulation described in the text (see also Fig. 6) for a $t = 200$ yr integration time. The emission from the undisturbed environment is not included in the CO 2-1 intensity map. The outflow is assumed to lie on the plane of the sky, and the maps have been convolved with a Gaussian point spread function of $\text{FWHM}=10^{15}$ cm to simulate the effects of the seeing. The maps are displayed with a linear grey scale. The intensity values which correspond to the different shades of grey are indicated to the right of each plot, with a value of 1 corresponding to the peak intensity of the corresponding map.

interesting constraints on the atomic/molecular composition of HH jets and/or on their jet-to-environment density ratios. For numerical simulations in which the jet is assumed to be partially molecular, we refer the reader to the work of Suttner et al. (1997) and Smith, Suttner & Yorke (1997).

Finally, we should note that the calculation of the $[S\ II]$ 6717+6731 emission coefficient was calculated by solving a five-level atom problem. The $H\alpha$ emission coefficient was computed including the contributions of the recombination cascade, as well as collisional excitations from the $n = 1$ level. The

H₂ 1-0 s(1) emission coefficient was computed by solving a multi-level molecule problem. These calculations are described in more detail in Raga et al. (1995). Finally, the CO 2-1 emission coefficient was computed assuming an LTE population for the excited levels of CO. As the undisturbed environmental gas emits quite strongly in this line, we have not included this emission in computing the CO 2-1 intensity map (Fig. 7).

4. Conclusions

We have shown that the separation between the bow and jet shocks of a radiative working surface is small compared to the jet radius. We therefore describe a very simple, thin shell model for the motion of a working surface of a jet with a non-top hat cross section. This cross section could either be the direct result of the ejection mechanism, or alternatively it could be a “self-generated” cross section resulting from the interaction of the jet beam with the surrounding environment.

This thin shell analytic model directly relates the shape of the curved working surface to the velocity and density cross sections of the jet. In particular, for the high jet-to-environment density ratio which is empirically found for many bow shock-like HH objects, we find that the shape of the working surface directly reflects the velocity cross section of the jet.

The curved working surfaces obtained for a non-top hat cross section, radiative jet result in a convergence of either the post-jet shock material (for convex working surfaces) or the post-bow shock material (for concave working surfaces). This convergence results in the formation of an on-axis “nose cone”. Once such a nose cone begins to form, the jet and bow shocks are forced apart from each other, so that the working surface cannot be described any more with a thin shell approximation.

Finally, we have carried out a full numerical simulation for a radiative, axisymmetric jet with top hat density and temperature cross sections, and with an axially peaked velocity cross section. This simulation shows that at early stages the numerical solution closely follows the analytic, thin shell solution. At later stages, a warm nose cone is formed (which is of course not described by the thin shell model).

The nose cone produced in this numerical simulation has interesting observational properties. The nose cone is visible in the predicted H α and [S II] intensity maps, and has a high [S II]/H α ratio. A structure that might correspond to such a nose cone has been observed in HH 47A by Heathcote et al. (1996).

If the jet were partially molecular, for many sets of parameters this nose cone would also emit strongly in molecular (e. g., H₂ and CO) lines. However, in our numerical simulation (in which we have assumed that the jet is atomic) the molecular emission is confined to the wings of the bow shock. A direct observation of molecular emission in the nose cone of an HH object would be clear evidence that the material in the jet beam is at least partially molecular.

In an axisymmetric simulation, the nose cone continues to grow in size and mass, and eventually develops a complex structure of internal shocks (Raga 1994). However, the 3D simulations of Suttner et al. (1997) show that a small perturbation in

the ejection direction of the jet results in a breakdown of the nose cone structure before it becomes very extended. Clearly, further studies should be carried out to clarify to what extent nose cone structures can be developed in 3D jets, and whether or not these structures are observed in HH objects.

Acknowledgements. The work of AR and JC has been supported by grants from CONACyT and the UNAM/ Cray Research Program. AR would like to thank the Observatoire de Paris for support for a visit to the Observatoire during which part of this work was carried out.

References

- Blondin, J. M., Fryxell, B. A., & Königl, A., 1990, *ApJ*, 360, 370.
 Cantó, J., Raga, A. C., & Binette, L. 1989, *Rev. Mex. Astron. Astrofis.*, 17, 65.
 Cantó, J., & Raga, A. C. 1991, *ApJ*, 372, 646.
 Dash, S. M., Wolf, D. E. & Seiner, J. M., 1985, *American Institute of Aeronautics and Astronautics Journal*, 23, 505.
 Davis, C. J., Eisloffel, J. & Ray, T. P., 1994, *ApJ*, 426, 93.
 Falle, S. A. E. G., 1994, *MNRAS*, 269, 607.
 Falle, S. A. E. G., Innes, D., and Wilson, M. J., 1987, *MNRAS*, 225, 741.
 Hartigan, P., Raymond, J. C., & Hartmann, L., 1987, *ApJ*, 316, 323.
 Heathcote S., Morse, J. A., Hartigan, P., Reipurth, B. et al., 1996, *AJ*, 112, 1141.
 Mellema, G., Raga, A. C., Cantó, J., Lundqvist et al., 1998, *A&A*, 331, 335.
 Noriega-Crespo, A., & Garnavich, P. M., 1994, *RMxAA*, 28, 173.
 Raga, A. C., 1988, *ApJ*, 335, 820.
 Raga, A. C., 1994, in *Stellar and Circumstellar Astrophysics*, eds. G. Wallerstein and A. Noriega-Crespo, *PASP Conf. Proc.*, 57, 85.
 Raga, A. C., 1995, in *Circumstellar disks, outflows and star formation*, eds. S. Lizano and J. M. Torrelles, *Rev. Mex. Astron. Astrofis. Conf. Ser.*, 1, 103.
 Raga, A. C., & Binette, L. 1991, *Rev. Mex. Astron. Astrofis.*, 22, 265.
 Raga, A. C., Cabrit, S., & Cantó, J., 1995, *MNRAS*, 273, 422.
 Raga, A. C., Mellema, G., & Lundqvist, P. 1997, *ApJS*, 109, 517.
 Raga, A. C., Taylor, S., Cabrit, S., & Biro, S., 1995, *A&A*, 296, 833.
 Smith, M. D., Suttner, G., & Yorke, H. W., 1997, *A&A*, 323, 223.
 Smith, M. D., Völker, R., Suttner, G., & Yorke, H. W., 1997, in *Herbig-Haro objects and low mass star formation*, eds. B. Reipurth and C. Bertout (Dordrecht, Reidel), p. 303.
 Suttner, G., Smith, M. D., Yorke, H. W., & Zinnecker, H., 1997, *A&A*, 318, 595.